





Synthesis, crystal and magnetic structure of the spin-chain compound Ag_2RuO_4

Beluvalli E. Prasad,¹ Surasree Sadhukhan,² Thomas C. Hansen ,³
 Claudia Felser ,¹ Sudipta Kanungo ,² and Martin Jansen ^{1,4,*}

¹Max-Planck-Institut für Chemische Physik fester Stoffe, Nöthnitzer Strasse 40, 01187 Dresden, Germany

²School of Physical Sciences, Indian Institute of Technology Goa, 403401 Goa, India

³Institut Max von Laue-Paul Langevin, 71 Avenue des Martyrs, 38000 Grenoble, France

⁴Max-Planck-Institut für Festkörperforschung, Heisenbergstrasse 1, 70569 Stuttgart, Germany



(Received 11 October 2019; accepted 2 January 2020; published 28 February 2020)

We report synthesis and crystal structure refinement of Ag_2RuO_4 , followed by combined analysis of its physical properties through bulk experimental tools (magnetic susceptibility, electron transport, and heat capacity measurements), a microscopic experimental tool (temperature dependent neutron diffraction), and *ab initio* first-principles calculations. We observe a rather unique $(\text{RuO}_{3/1}\text{O}_{2/2})_n$ polyoxoanion, where Ru is in a distorted trigonal bipyramidal coordination by oxygen. The RuO_5 polyhedra are linked via the apical oxygen atoms to form chains extending along the crystallographic *a* axis. Crystal structure, magnetization, and *ab initio* calculations indicate that Ru is in the +6 oxidation state with a nominal valence electron configuration of $4d^2$. Bulk magnetization, specific-heat, and neutron-diffraction measurements provide clear indication of an antiferromagnetic transition around 75 K with moderate spin canting in the order of 30° with respect to the *c* axis. The neutron-diffraction results as well as the density functional theory based first-principles calculations of exchange interactions revealed that the strong intrachain interaction is predominantly of ferromagnetic (FM) type, and that this spin order along the chains couples with the neighboring chains through comparatively weak FM and antiferromagnetic interactions. Notably, the Landé *g* factor is found to be 1.8 (with an infinite chain model and even a simple Curie-Weiss approach), away from the ideal value of 2, due to the low dimensionality of the Ru/O substructure.

DOI: [10.1103/PhysRevMaterials.4.024418](https://doi.org/10.1103/PhysRevMaterials.4.024418)

I. INTRODUCTION

Low-dimensional quantum magnets constitute a highly rated and investigated topic in the condensed matter community due to their versatile novel features [1], such as a Haldane gap [2] in the $S = 1$ spin-chain compound $\text{Ni}(\text{C}_5\text{H}_{14}\text{N}_2)_2\text{N}_3(\text{PF}_6)$ [3], gapless magnetic excitation in $S = \frac{1}{2}$ Heisenberg antiferromagnetic (AFM) chains [4], spin dimerization, unconventional spin excitations, quantum criticality [5,6], a spin-Peierls transition in CeCuGe_3 [7], a quantum spin-liquid state in κ -(BEDT-TTF) $_2\text{Cu}_2(\text{CN})_3$ [8,9], or a bilayer magnet in $\text{Ca}_{10}\text{Cr}_7\text{O}_{28}$ [10]. Although these materials are structurally three dimensional, the effective low dimensionality in this context arises because of the strong directional character of the crystal structure, where unique arrangements of the constituent magnetic ions induce anisotropic electronic and magnetic interactions. In the past, the main focus was on $3d$ transition-metal (TM) based systems. More recently, ternary oxides with heavy TMs ($4d$ and $5d$) have attracted particular attention due to the possibilities of the intimate interplay between electron-electron correlation, spin-orbit coupling (SOC), and crystal-field splitting,

which are in a comparable energy scale for $4d$ and $5d$ TMs. Whereas the $5d$ iridates have been studied extensively in the context of low-dimensional magnets in the form of Heisenberg-Kitaev spin liquids [11,12] and $J_{\text{eff}} = \frac{1}{2}$ spin-orbit coupled Mott insulators in layered iridates [13,14], $4d$ TM based ternary oxides are comparatively less investigated in this respect. Nonetheless, among the $4d$ TMO's, ruthenates exhibit extraordinary properties in terms of both structural aspects as well as electronic and magnetic responses. The binary oxide RuO_2 [15] is a metallic conductor with Pauli paramagnetism; the perovskite-type ternary SrRuO_3 , CaRuO_3 , and BaRuO_3 show metallic conduction with ferromagnetism below 165 K, are paramagnetic metals down to 4 K with AFM interactions, and adopt varied magnetic states depending on the synthesis conditions [16–21]; while Sr_2RuO_4 [22] exhibits unconventional *p*-type superconductivity. In the context of low-dimensional magnets ruthenates have come into the picture with the discovery of layered α - RuCl_3 [23,24] as a spin-liquid system, followed by one-dimensional (1D) Li_3RuO_4 [25,26] and two-dimensional Li_2RuO_3 [27–29] materials.

We are interested in new low-dimensional topologies of ruthenates with different arrangements of magnetic Ru ions in higher oxidation states, compared to Ru^{+4} or Ru^{+5} as discussed above. Such phases may give rise to quantum fluctuations due to small spin values and to various interesting ground-state magnetic properties. However, from the synthesis point of view achieving such a goal is not trivial. Our strategy is to play with the charge compensating counterions in ternary oxoruthenates. Here, the alkali-metal and alkaline-earth cations are commonly first choice, due to

*Corresponding author: m.jansen@fkf.mpg.de

Published by the American Physical Society under the terms of the [Creative Commons Attribution 4.0 International license](https://creativecommons.org/licenses/by/4.0/). Further distribution of this work must maintain attribution to the author(s) and the published article's title, journal citation, and DOI. Open access publication funded by the Max Planck Society.

two complexions, namely, by the expectation that the high oxide basicities [30,31] of such binary oxides would foster solid-state reactivity, and that the “innocent” character of the alkali-metal and alkaline-earth cations would not impose a steric strain to the crystal structures forming and would demand nothing but an adequate share of space. Given such a matrix, the second constituting cation would be given freedom to develop a large variety of compositions, valence states, and electronic structures. The choice in alternative monovalent cations—which are essentially Cu^{1+} , Ag^{1+} , or Tl^{1+} —is but scarce, and each of them poses particular challenges when involved in solid-state syntheses. For silver(I) oxide, its low thermal stability constitutes a crucial impediment. This handicap, however, has been overcome by maintaining a sufficiently high oxygen pressure during solid-state reaction of couples of respective binary oxides [32]. Using autoclaves, capable of enduring oxygen pressures and temperatures of about 0.7 GPa and 700 °C, has opened a particularly valuable parameter window for reacting silver(I) oxide with virtually any binary oxide in the periodic table, thus enabling researchers to explore wide areas for unknown materials experimentally.

Since the effective radii of Ag^{1+} and of Na^{1+} are comparable in size, one would expect to encounter lots of similarities between silver and sodium oxometallates. However, in contrast, most of the time for the same composition distinctly different structures and properties were revealed. Of course, the inclination of Ag^{1+} to form more covalent bonds to oxygen and to strive for low coordination numbers is relevant in this context, but in addition new appreciably structure directing characteristics have been disclosed. Noteworthy, the equally charged silver cations tend to aggregate to clusterlike extended assemblies with interatomic separations in the same range as found for elemental silver, and even below [33]. Such weakly attractive (metallophilic) d^{10} - d^{10} interactions have a significant effect on the structural evolutions [34,35], and give rise to special transport properties [36] and visible light absorption [37].

Utilizing high-oxygen-pressure and hydrothermal synthesis techniques, we started to explore $\text{Ag}_2\text{O}/\text{RuO}_x$ systems, which has resulted in the discovery of several silver ruthenates. Among them, AgRuO_3 shows strong antiferromagnetic exchange coupling on a $[\text{RuO}_3]$ honeycomb lattice [38], α - Ag_3RuO_4 forms a 1D polyoxoanion of edge-sharing octahedra [39], while the β polymorph features an oligomeric oxoanion [40]. The latter representative is kind of exceptional in as much it is closely related to the sodium analog, containing the same tetrameric oxoanion [41–43], showing frustrated-magnetic exchange coupling within the tetrameric spin cluster [40,43].

Here, we report on synthesis, crystal structure, and details of magnetic structure of Ag_2RuO_4 , which likewise is related to the sodium analog [44–47]. Ag_2RuO_4 was mentioned for the first time back in 1967, when Nowogrocki, working on ruthenates(VI) and ruthenates(VII), signaled the synthesis of the title compound by precipitation out of an aqueous solution of potassium per-ruthenate(VII) with a soluble salt of silver(I) [48]. Samples prepared along this route show the same crystal structure as found for the title compound.

We investigated Ag_2RuO_4 through macroscopic measurements like magnetic susceptibility, electron transport, and

heat capacity measurements, a microscopic experimental tool of temperature-dependent neutron-diffraction and *ab initio* first-principles calculations. The analysis shows a chain-type polyoxoanion consisting of trigonal bipyramidal $[\text{RuO}_5]$ primary building units sharing the apical vertices, forming chains along the crystallographic a axis. Thus, Ag_2RuO_4 belongs to the class of low-dimensional quantum magnets. It shows a clear AFM transition at around 75 K, with moderate spin canting. Electronic structure calculations revealed that strong intrachain interaction among the Ru^{+6} ($4d^2$) is predominantly ferromagnetic. Remarkably, the sister compound of Ag_2RuO_4 , i.e., Na_2RuO_4 , although structurally quite similar, shows a different interesting anisotropic quasi-1D nature magnetic structure [45,47].

II. EXPERIMENTAL

A. Synthesis

The title compound was synthesized from Ag_2O (freshly precipitated with KOH from an aqueous solution of AgNO_3) and KRuO_4 (Alfa Aesar 97%) by applying hydrothermal conditions using a Teflon-lined stainless-steel autoclave. For a typical batch of about 150 mg, Ag_2O and KRuO_4 in the required molar ratio of 1:1 were added to 8 ml of deionized water, the mixture was stirred subsequently for 10–15 min, placed in a 25-ml autoclave, and heated to 140–150 °C for 48–72 h. After switching off the heating source, the autoclave was allowed to cool to room temperature. The product formed was filtered off, washed with deionized water and ethanol, and finally dried in a desiccator.

B. Thermal analysis

The thermal stability of the title compound was monitored by thermogravimetric analysis (TGA)/differential thermal analysis (DTA) (NETZSCH STA 449 °C, argon atmosphere, flow rate 100 ml/min, heating rate 10 K/min).

C. X-ray and neutron powder diffraction

A powder pattern of the sample was recorded by x-ray diffraction (Huber, G670, $\text{Cu-K}\alpha_1$ radiation, $\lambda = 1.54056 \text{ \AA}$). Rietveld refinement of the x-ray powder pattern was carried out using the program TOPAS-V4.2.0.2 [49] (Fig. 1). Neutron powder-diffraction experiments were performed at the high intensity diffractometer D20 at ILL, Grenoble [50]. For confirmation of the nuclear structure, a high-resolution configuration was used with a wavelength of 1.48 Å obtained from the (335) reflection of a germanium monochromator at 118° takeoff angle. Patterns were acquired at room temperature (296 K), just above the magnetic transition temperature (76 K), and the cryostat’s base temperature of 1.8 K.

For the precise, unambiguous determination of the magnetic structure a high intensity configuration was used with a wavelength of 2.41 Å from the (002) reflection of a highly oriented pyrolytic graphite monochromator. A thermodiffraction experiment was performed in this configuration with data acquisitions of 2 min each with the stationary 153.6°-covering position sensitive detector. The temperature was raised from 1.8 to 76 K at a rate of 2.5 K per data acquisition, and another one from ≈ 1.8 to 113.4 K at a rate of ≈ 1.1 K

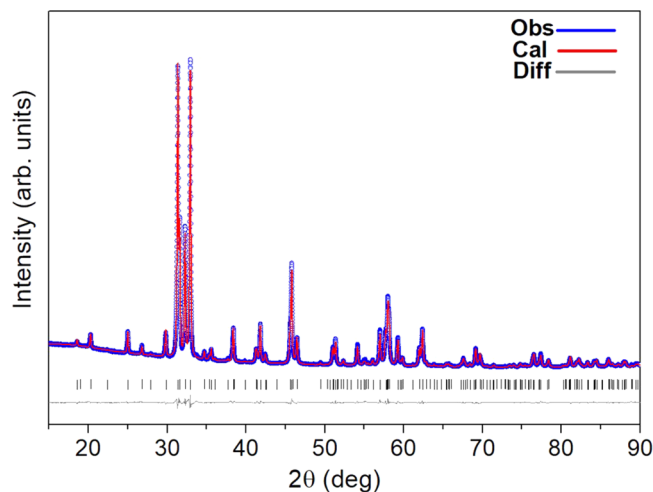


FIG. 1. Rietveld fit of the PXRD pattern of Ag_2RuO_4 .

per data acquisition, in order to follow the temperature dependence of the magnetic moment. Particularly long acquisitions were performed at 1.8 and 76 K (just above the magnetic ordering temperature), with 10 h of counting time each, using a detector scan for more precision (excluding parasitic signals and faulty detector efficiencies), two scans for each temperature, covering 3° with a step width of 0.05° with 5 min counting time per step.

D. Measurement of physical properties

Magnetization was measured in an MPMS-XL7 magnetometer (Quantum Design) between 1.8 and 400 K. The electrical resistivity was recorded on a powder sample pressed in a sapphire die cell with four Pt contacts using the van der Pauw method and reversing direct current. Heat capacity was determined in the temperature range 1.8–300 K (HC option, PPMS, Quantum Design).

E. Computational methods

In order to characterize the electronic structure and magnetic properties, density functional theory (DFT) based investigations were carried out using the low-temperature (1.8 K) neutron-diffraction crystal structure, within the plane-wave basis set based on a pseudopotential framework as implemented in the Vienna *ab initio* simulation package VASP [51,52]. The exchange-correlation functional was chosen to be the generalized gradient approximation (GGA) following the Perdew-Burke-Ernzerhof prescription [53]. The missing electronic correlation beyond the standard GGA, which is necessary for a transition-metal ion such as Ru, was accounted for by using Hubbard on-site coulomb correlation as implemented in the GGA + U method [54,55], with a choice of the Hubbard ($U = 2.9$ eV) and Hund's coupling ($J_H = 0.9$ eV) at the Ru site, thus considering values commonly applied for ruthenate compounds. The results shown are for $U = 2.9$ eV and $J_H = 0.9$ eV. We also crosschecked the influence on our results by varying the U_{eff} values in the range of 1 to 4 eV. We optimized the experimental crystal structure by relaxing the position of each atom up to 0.005 eV/Å in the

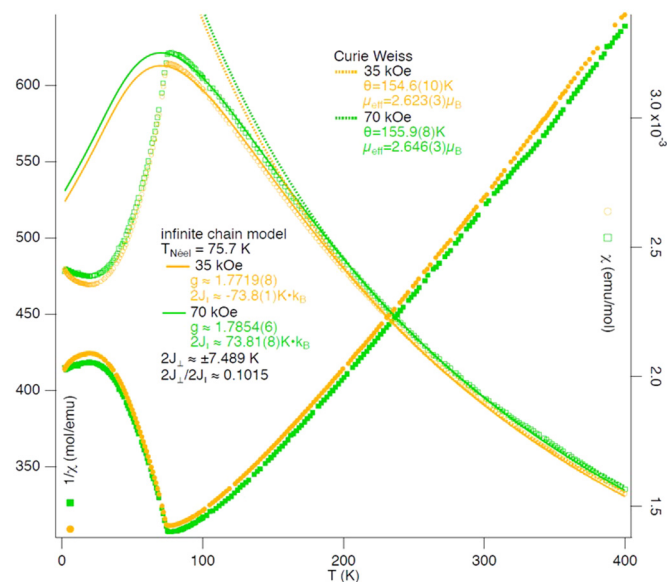


FIG. 2. Magnetic susceptibility (empty squares and circles) and inverse susceptibility (filled squares and circles) measured in an applied field of 70 kOe (green squares) and 35 kOe (orange circles). The solid lines represent fits of the data in the range from 75 to 400 K calculated with a model for isolated chains of classical spins with refined parameters $2J_{\parallel} \approx -74$ K and $g \approx 1.8$. The dotted lines represent fits with the Curie-Weiss law. All data were recorded in FC mode.

unit cell, keeping the lattice parameters the same as obtained from the neutron-diffraction measurement. For self-consistent calculations we used an electronic convergence criterion of 10^{-7} eV and a $6 \times 6 \times 6$ mesh division for the Brillouin-zone integration.

III. RESULTS

A. Synthesis and bulk properties

Ag_2RuO_4 was synthesized along an improved synthetic route, namely, from Ag_2O and KRuO_4 , applying hydrothermal conditions. As evidenced by powder x-ray diffraction (PXRD) (Fig. 1), the solid formed is single phased and of good crystallinity. The shiny-black product is insensitive to air and moisture, and starts decomposing at 360°C , according to simultaneous DTA/TGA (Fig. S1 in Supplemental Material [56]). The weight loss (8.4%) during the first step of decomposition corresponds to the mass of two equivalents of oxygen. The solid residual was characterized by PXRD, and consists of metallic silver and RuO_2 .

The susceptibility of the sample measured as a function of temperature in an applied field of 70 and 35 kOe (Fig. S2 [56]) indicates AFM exchange coupling with magnetic ordering occurring at $T_N = 75.4$ K. The effective magnetic moment calculated by fitting the Curie-Weiss law in the temperature range 200–375 K amounts to $2.6 \mu_B$ (Fig. 2) and is close to the spin-only moment of Ru^{6+} . Deviations of $\chi^{-1}(T)$ from linearity at approaching T_N may be attributed to weak frustration effects.

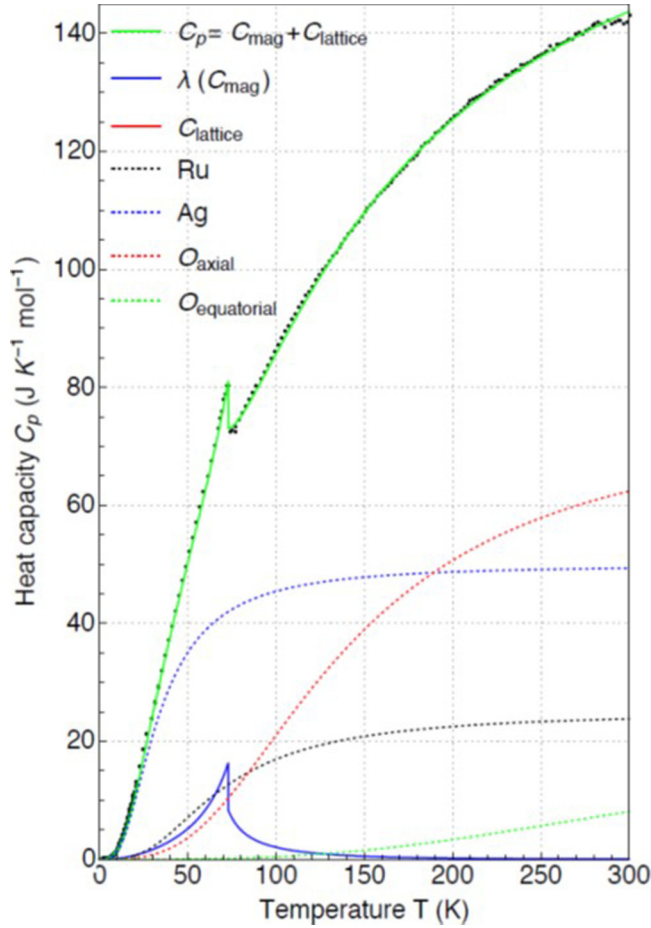


FIG. 3. Heat capacity C_p (experimental, black dots) fitted (green) by a lattice contribution C_{lattice} as a sum (red) of four Debye functions (dotted) and a λ function for the magnetic contribution C_{mag} (blue).

Heat capacity measured as a function of temperature (Fig. 3) shows an anomaly at about 75 K, which confirms the phase transition observed in the magnetic study. We fitted the heat capacity data applying a linear combination of four Debye functions with Debye temperatures of 138(2), 289(14), 582(5), and 1615(18) K, corresponding to the lattice contribution of the formula unit (two Ag, one Ru, three equatorial, and one axial O position) and an empiric lambda function [57]. The latter represents the magnetic contribution C_{mag} to the heat capacity C_p and is defined below and above the Néel temperature $T_{\text{Néel}}$ as follows, with the semiempirical parameters K_m , K_n , m , and n as presented in Ref. [57]:

$$\begin{aligned}
 T < T_{\text{Néel}} : & 2RK_m \ln \left[\frac{1 + \left(\frac{T}{T_{\text{Néel}}}\right)^m}{1 - \left(\frac{T}{T_{\text{Néel}}}\right)^m} \right] \\
 & \approx 2RK_m \left[\left(\frac{T}{T_{\text{Néel}}}\right)^m + \frac{1}{3} \left(\frac{T}{T_{\text{Néel}}}\right)^{3m} + \frac{1}{5} \left(\frac{T}{T_{\text{Néel}}}\right)^{5m} \right], \\
 T > T_{\text{Néel}} : & 2RK_n \ln \left[\frac{\left(\frac{T}{T_{\text{Néel}}}\right)^n + 1}{\left(\frac{T}{T_{\text{Néel}}}\right)^n - 1} \right] \\
 & \approx 2RK_m \left[\left(\frac{T}{T_{\text{Néel}}}\right)^{-n} + \frac{1}{3} \left(\frac{T}{T_{\text{Néel}}}\right)^{-3n} + \frac{1}{5} \left(\frac{T}{T_{\text{Néel}}}\right)^{-5n} \right].
 \end{aligned}$$

A reasonable fit has been obtained with $K_m = 0.65(27)$, $K_n = 0.32(18)$, $m = 2.1(4)$, $n = 3.2(1.3)$, and $T_{\text{Néel}} = 73(7)$ K. In both cases, the integration over T of this supposed λ -shaped heat capacity anomaly around the Néel temperature, $C_{\text{mag},\lambda}/T$, delivers a value for the magnetic entropy of $S_{\text{mag}} \approx 8.4 \text{ J K}^{-1} \text{ mol}^{-1}$ instead of an expected value of $S_{\text{mag}} = R \ln(2S + 1) \approx 9.1 \text{ J K}^{-1} \text{ mol}^{-1}$. Yet, regarding the empiric character of the fit and the lack of a model fitting a non-negligible shoulder in the heat capacity, once the lattice contribution is subtracted, at ≈ 15 K, the value is sufficiently close to the theoretical one, to confirm the model, notably $S = 1$.

The electrical resistivity (Fig. S3 [56]) measured as a function of temperature confirms the semiconducting nature of the compound. The low-temperature part of conductivity can be fitted by a variable range hopping model $\sigma = \sigma_0 \exp[-(T_0/T)^\beta]$ with $\beta = 1/4$, and a Mott temperature of $T_0 \approx 30$ K.

B. Crystal structure

The crystal structure of Ag_2RuO_4 was solved and refined using neutron and x-ray powder data. The crystallographic details of the structure determination, the atomic parameters, and the relevant distances and angles are given in Tables I, S1 [56], and II, respectively. According to the quite consistent results of the set of structure refinements performed, ruthenium is in a fivefold, trigonal bipyramidal coordination by oxygen. The apical oxygen atoms of the bipyramids connect to form infinite chains $\text{RuO}_{3/1}\text{O}_{2/2}$ along the a direction (Fig. 4).

The Ru-O bond distances vary from 1.752 to 1.776 Å for equatorial and from 1.984 to 2.007 Å for apical oxygen atoms, respectively. The O-Ru-O angles along the chain directions are nearly linear (179.72°), while the bipyramids are appreciably tilted with respect to neighboring polyhedra, as is indicated by a Ru-O-Ru angle of 125.64° . As illustrated by Figs. 4 and 5, the silver atoms are arranged to form approximately hexagonal tubes aligned parallel along [100] establishing a honeycomblike pattern. The tubes are centered by the Ru/O chains, which thus form an almost ideal hexagonal rod packing. The individual rods are linked by silver atoms which are coordinated by five oxygen atoms, with the Ag-O bond distances ranging from 2.356 to 2.475 Å (Fig. 5). Further, Figs. S4 [56], 4, and 5 display corresponding details of the crystal structures of Ag_2RuO_4 and Na_2RuO_4 for comparison, revealing a close relationship of the two structures.

C. Magnetic ordering

Upon cooling the sample below $T_N \sim 75.4$ K, the appearance of new reflections in the neutron-diffraction patterns indicates the onset of long-range magnetic ordering of the Ru^{6+} ions. Figure S5 [56] shows the diffraction patterns of Ag_2RuO_4 collected with the diffractometer D20 at two different temperatures: $T = 76$ K (just above the magnetic transition temperature, lower curve) and $T = 1.8$ K (saturated magnetic state). The total Bragg intensity at $T = 76$ K is originating from nuclear scattering by the atoms of the chemical cell of Ag_2RuO_4 . The additional reflections visible at $T = 1.8$ K, on the other hand, are of magnetic origin.

TABLE I. Crystallographic data and refinement details from PXRD and neutron powder diffraction (NPD).

Compound	Ag ₂ RuO ₄			
Diffraction mode	PXRD	NPD	NPD	NPD
Wavelength	1.5406 Å	1.4773 Å	1.4773 Å	1.4773 Å
Temperature	298 K	296 K	76 K	1.8 K
Formula weight	380.80			
Space group (no.)	<i>Pnma</i> (62)			
Lattice constants				
<i>a</i> (Å)	7.1020(1)	7.1018(3)	7.0827(3)	7.0855(2)
<i>b</i> (Å)	9.3370(2)	9.3363(4)	9.2992(4)	9.2987(3)
<i>c</i> (Å)	5.5353(1)	5.5355(2)	5.5164(2)	5.5150(2)
<i>V</i> (Å ³)	367.05 (1)	367.03 (3)	363.33 (2)	363.36 (2)
Rp / Rwp	0.0293/0.0467	0.047/0.049	0.039/0.044	0.040/0.045
Goodness of fit	2.36	2.79	3.07	3.38

All additional lines originating from the neutron diffraction on the system of ordered Ru⁶⁺ magnetic moments can be indexed with integer indices within the parent unit cell of the crystal structure of Ag₂RuO₄. This implies a propagation vector of the magnetic structure of $\kappa = (000)$. The confirmation of the propagation vector was performed using the search routine K-SEARCH which is part of the FULLPROF suite [58]. This propagation vector, together with the known crystal symmetry of the chemical cell, and the positions of the Ru⁶⁺ magnetic ions, serve as an input for the symmetry analysis of the possible magnetic ordering schemes. The representation analysis of the low-temperature magnetic structure was carried out with the Program BASIREPS (part of the FULLPROF suite). All predicted symmetry-allowed spin configurations have been checked with Rietveld refinements by FULLPROF [59]. Very clearly, only one out of the eight irreducible representations (Γ_6 for the Ru⁶⁺ ions in the notation of BASIREPS), which has two basis vectors, (100) and (001), provides sets of calculated diffraction peaks consistent with our experimental data. The corresponding magnetic space group (Shubnikov group) is *Pnma*. In this structure, the Ru⁶⁺ ions are coupled ferromagnetically along the chain direction [100], concerning the main component to the magnetic moment vector, pointing in direction [001], and antiferromagnetically concerning the

minor component in the chain direction [100]. The chains are coupled antiferromagnetically (concerning the main component, ferromagnetically concerning the minor component) to the four closest chains in the *b-c* plane and totally ferromagnetically to the two, by 3% farther chains in direction [001]. Out of the other irreducible representations, six do not explain the presence of the strong (010) and another one predicts intensity where none is observed. All possibilities of purely ferromagnetically ordered chains have been checked and could be excluded. One should note here that the chains are arranged pseudo-hexagonally. From Fig. S9 [56] one can state another important difference of the two farther neighbor chains in [001] as compared to the four closer ones: The two farther chains have the same orientation, whereas the four closer ones are “undulated” differently. As visible from Fig. S6 [56], the orientation of vectors with respect to the chains is different in Na₂RuO₄, where all chains are ferromagnetically arranged to each other, while the intrachain coupling is AFM.

The magnetic structures described by the two combinations (“± ±” and “± ∓”—referring to the signs of the moment vector of the first Ru position in Table III) of the two basis vectors differ only in the direction of the magnetic moment with respect to the oxygen coordination of Ru⁶⁺ in the

TABLE II. Bond lengths (Å) and angles (°) (including those for Na₂RuO₄ from NPD at 293 K for comparison [44]).

M-O (Ag ₂ RuO ₄)	X ray	NPD (296 K)	NPD (1.8 K)	Na ₂ RuO ₄ (Ru1)	NPD (Ru2)
Ru-O2	1.752(9)	1.755(2)	1.764(2)	1.77(1)	1.782(7)
O3 (× 2)	1.776(9)	1.776(1)	1.782(1)	1.78(1)/1.80(1)	1.77(1)/1.79(1)
O1	1.984(4)	1.995(2)	1.990(2)	1.975(7)	1.997(6)
O1	2.007(4)	2.003(2)	2.003(2)	1.982(7)	1.998(6)
Ag-O1	2.356(6)	2.349(1)	2.342(1)		
O3	2.439(7)	2.452(1)	2.430(1)		
O3	2.456(6)	2.455(1)	2.434(1)		
O3	2.460(7)	2.456(1)	2.440(1)		
O2	2.475(7)	2.471(1)	2.460(1)		
Angles	X ray	NPD (296 K)	NPD (1.8 K)	Na ₂ RuO ₄ (Ru1/O7)	Na ₂ RuO ₄ (Ru2/O8)
O1-Ru-O1	179.72 (5)	179.9 (1)	180.0 (1)	179.3 (4)	178.9 (4)
Ru-O1-Ru	125.64 (4)	125.3 (1)	125.06 (9)	124.4 (5)	123.3 (4)

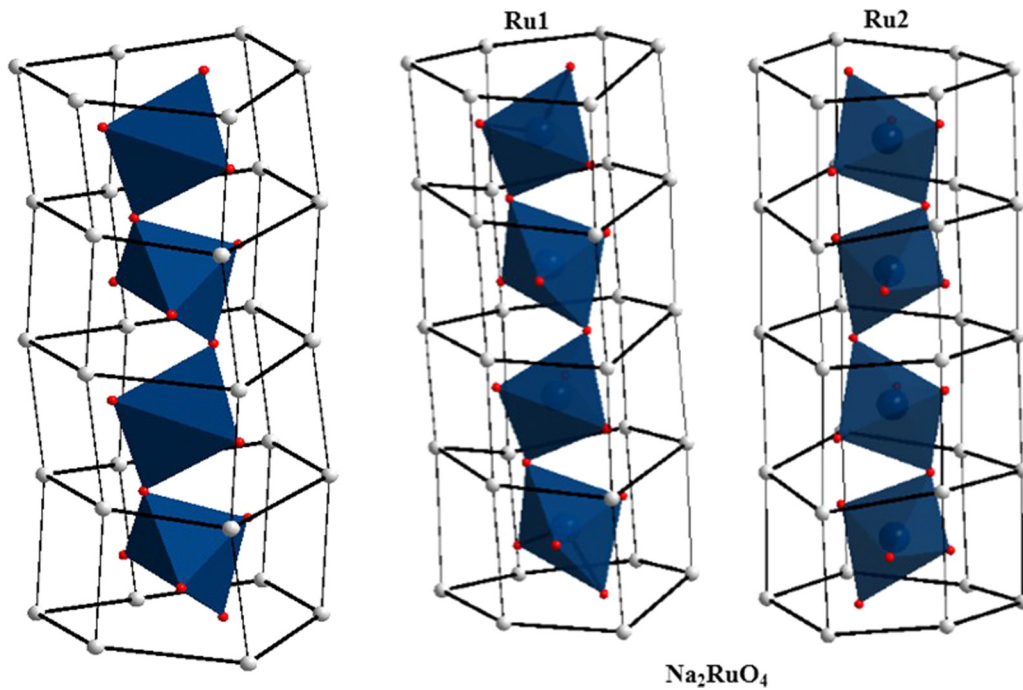


FIG. 4. Visualization of individual (RuO₅) chains and the surrounding monovalent countercations for Ag₂RuO₄ (left) and for Na₂RuO₄ (right), where the two columns correspond to the independent Ru1 (left) and Ru2 (right) sites. RuO₅ polyhedra: blue, oxygen; red spheres, silver; gray spheres, sodium.

chemical cell, pointing in the trigonal base plane of the trigonal bipyramids or out of it, respectively. Precise checking of these two possibilities has shown that the difference is non-significant in any diffraction experiment, as Ru⁶⁺ occupies nearly (within 3σ) the ideal position (1/4 1/4 1/4), where a shift of the magnetic unit cell by [1/2 0 0] becomes possible without altering diffraction intensities at all. However, in Na₂RuO₄, the vectors lay inside the plane, as Fig. S6 [56] shows; by analogy, one can conclude that this orientation is also the most likely one in the case of Ag₂RuO₄. The refined components of magnetic moments along *a* and *c* stay roughly in the same proportion at all temperatures. The magnetic moment

lies in the *a-c* plane and is aligned predominantly along *c* with a weaker *a* component. At 1.8 K, the two components are refined to $M_c = 1.45(2)\mu_B$ and $M_a = 0.76(1)\mu_B$; in spherical coordinates, this corresponds to a magnetic moment of $M = 1.547(7)\mu_B$ at an angle $\Theta = 29.7(4)^\circ$ from the *c* axis. An illustration of the two possible magnetic structure models for Ag₂RuO₄ is shown in Fig. 6. There is only one irreducible representation fitting the diffraction data, and the absolute amount of the two basis vectors it contains converges to reproducible values of M_a and M_c . Yet, the signs of the two basis vectors relative to each other are interchangeable. Due to the pseudosymmetry described above, the two slightly

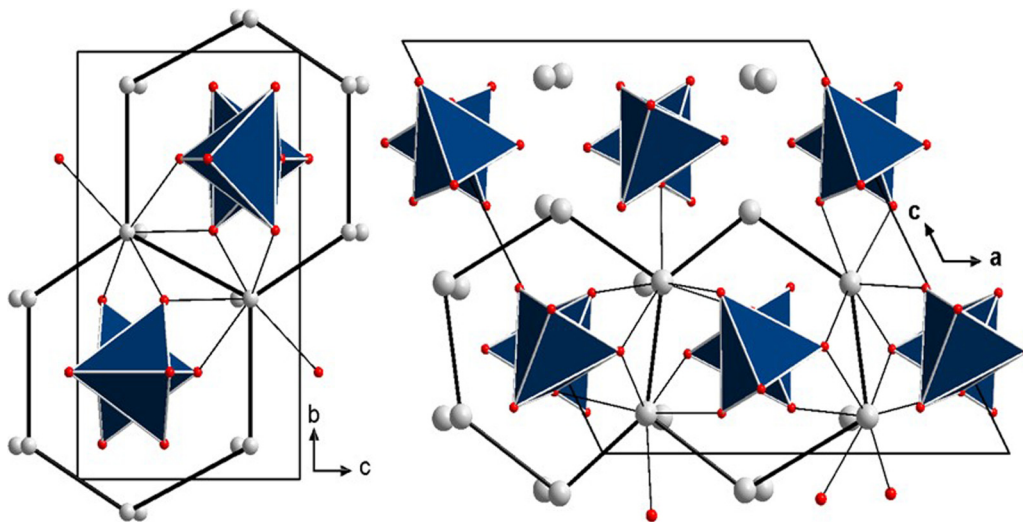


FIG. 5. Connectivity between (RuO₅) chains in Ag₂RuO₄ (left) and Na₂RuO₄ (right) as mediated by Na⁺ and Ag⁺, respectively. Thin black lines cover distance ranges from 2.356 to 2.477 Å. Same color code as in Fig. 4.

TABLE III. Magnetic moment vectors for the four equivalent Ru positions ($x \approx -0.2497$, $z \approx -0.2506$, $M_a \approx 0.76 \mu_B$, $M_c \approx 1.45 \mu_B$, $M \approx 1.55 \mu_B$, $\Theta \approx 30^\circ$).

Ion	Fractional coordinates			Cartesian vector		Polar vector	
Ru1	$+x$	$\frac{3}{4}$	$+z$	$+M_a$	$\pm M_c$	$+M$	$\pm\Theta$
Ru2	$-x + \frac{1}{2}$	$\frac{1}{4}$	$+z + \frac{1}{2}$	$+M_a$	$\mp M_c$	$+M$	$\mp\Theta + 180^\circ$
Ru3	$-x$	$\frac{1}{4}$	$-z$	$-M_a$	$\mp M_c$	$+M$	$\pm\Theta + 180^\circ$
Ru4	$+x + \frac{1}{2}$	$\frac{3}{4}$	$-z + \frac{1}{2}$	$-M_a$	$\pm M_c$	$+M$	$\mp\Theta$

different magnetic structures are virtually undistinguishable and can (nearly) be transformed into each other by a simple translation. The chemical environment, however, is different for both solutions; however, in the diffraction experiment, there is no observable interference between the nuclear and the magnetic diffraction.

An additional difficulty in refining the exact value of the magnetic moment arises from the unknown magnetic form factor of thermal neutron scattering for the Ru^{6+} ions ($4d^2$ electronic configurations). To our knowledge, it has never been measured, or calculated to date. All modern Rietveld refinement codes use the approximations for the magnetic form factors as tabulated in Ref. [60], which only contains form factors for the atom Ru and the cation Ru^+ , but not for higher oxidation states. Obviously, these approximations cannot be used for the Ru^{6+} ion, since its outer electronic shells are much more strongly localized. If one tries the refinement with either of the two form factors, immediately an artificial unphysical “overall thermal parameter” for the magnetic phase needs to be introduced in order to obtain a reasonable fit quality. The exact determination of the Ru^{6+} form factor is beyond the scope of this investigation, therefore the same approach as in Ref. [45] was used: The magnetic form

factors of various lighter neighboring $4d$ elements in different oxidation states have been used in the refinement, and the best profile description (without necessity for any artificial overall thermal parameter for the magnetic phase) has been retained. The ion Zr^+ turned out to be the best candidate, in contrast to Ref. [45], where the Y atom form factor had been chosen. With the assumption of a slight preferred orientation of particles adopting the pseudohexagonal habit (needles or platelets) and a correction after March, the Y atom gives a better fit, but only with a considerable—and unlikely—texture correction (needle habit), and an unexpectedly high magnetic moment. Hence, we have used the known and tabulated approximation for the Zr^+ magnetic form factor in our refinements. Thanks to our high counting statistics in the difference pattern, the differences between different candidates in the Rietveld fit are significant, which gives us confidence that the approximation by Zr^+ can be considered as the closest possible and therefore delivers best possible absolute values for the magnetic moment.

In order to estimate the possible uncertainty in the determination of the absolute value of the Ru^{6+} magnetic moment, it is worth comparing the refined values for different trial magnetic ions. Without preferred orientation (the refinement

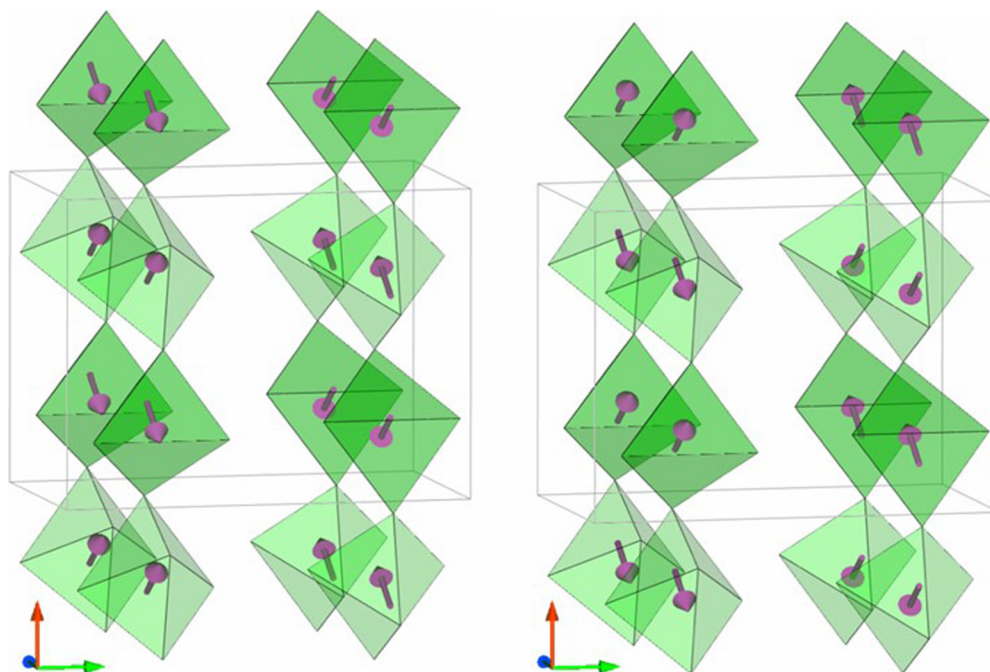


FIG. 6. Projection of the two possible magnetic structures of Ag_2RuO_4 along $[001]$, the a axis (direction of the chains $[100]$) pointing upwards in the paper plane. Only the unit-cell boundary, the $[\text{RuO}_5]$ coordination bipyramids around Ru^{6+} (green), and the magnetic moment vectors (purple) are represented. Crystallographic axes are indicated in red (a), green (b), and blue (c).

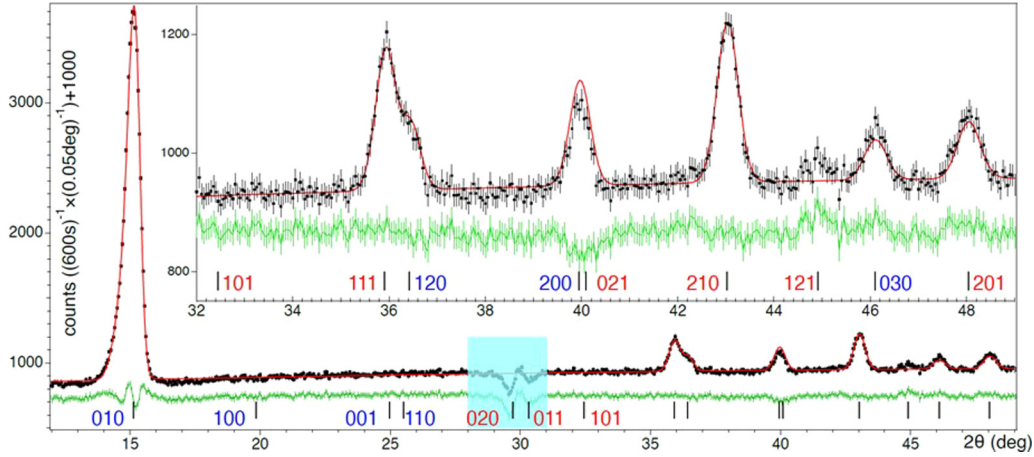


FIG. 7. Rietveld fit of the difference pattern (pattern at 1.8 K minus isotropic thermal expansion-corrected pattern at 76 K, black dots—an offset of 1000 counts has been applied) with the pure magnetic phase. Positions of strong nuclear peaks are excluded because of a remaining misfit due to thermal expansion. Black lines indicate Bragg peak positions; the corresponding indexing is given in blue for pure magnetic peaks, and in red for nuclear peaks with potential magnetic scattering contribution. The peaks (111), (021), (210), and (201) are at the position of a stronger nuclear peak, whereas one observes no magnetic scattering intensity at the peak positions (020), (011), (101), and (121). The latter seems to be of nonzero magnetic scattering intensity in the difference pattern for reasons of counting statistics (the nuclear scattering intensity is about three times as high as the magnetic peak (210)), thermal expansion, and the Debye-Waller factor.

of the full pattern, including magnetic and nuclear structure, gives no hint for a significant deviation from random orientation), they range from $1.455(6)\mu_B$ for Mo^+ ($\chi^2 = 2.28$), $1.494(6)\mu_B$ for Nb^+ ($\chi^2 = 2.05$), and $1.547(7)\mu_B$ for Zr^+ ($\chi^2 = 2.01$) to $1.635(6)\mu_B$ for Y ($\chi^2 = 2.25$). While (without the assumption of texture) Mo^+ and Y can be clearly excluded due to lack of fitting quality, the discrepancy of the values obtained with Nb^+ and Zr^+ gives an estimate of the uncertainty of the absolute value of the magnetic moment of less than $\pm 5\%$. Thus, we shall retain the value for Zr^+ in the following.

D. Temperature dependence and magnetostriction

The powder-diffraction refinement on the difference pattern is shown in Fig. 7. From respective refinements at various temperatures, the temperature dependence of the ordered magnetic Ru^{6+} moment magnitude has been extracted; it is presented in Fig. 8. In order to estimate the AFM transition temperature, the data of $M_{\text{Ru}}(T)$ shown in Fig. 8 were fitted to an empirical formula (1):

$$M_{\text{Ru}}(T) = M_0[1 - (T/T_N)^\alpha]^\beta. \quad (1)$$

The four free parameters refine to a saturated magnetic moment at $T = 0$ of $M_0 = 1.53(1)\mu_B$, a Néel temperature of $T_N = 75.8(4)$, and the exponents $\alpha = 3.3(5)$ and $\beta = 0.35(6)$. The inclination of the moment vector with respect to the c axis stays constant over temperature with $\Theta = 30.5(4)^\circ$, in agreement with $M = 1.547(7)\mu_B$ and $\Theta = 29.7(4)$ obtained from the refinement of the difference pattern at base temperature.

It is worth investigating potential magnetoelastic effects. Indeed, there is a clear discontinuity of lattice constants and unit-cell volume below the Néel temperature. One can fit the lattice constants above T_N to a modified Einstein function:

$$x(T) = x_0 + (E_0 + E_1x + E_2x^2)/[\exp(\theta_E/T) - 1]. \quad (2)$$

Below T_N one observes a strong negative deviation from the Einstein fit, for the lattice constants b and c and the unit-cell volume V , whereas the effect is insignificantly positive on the lattice constant a , as visible in Fig. S7 [56].

The unit-cell volume has been modeled in addition by a linear combination of four Debye functions with Debye temperatures of 138, 289, 582, and 1615 K, in analogy to and as obtained from the fit of the heat capacity data (Fig. 3) considering a unique proportionality parameter γ/B_0 (Grüneisen/bulk modulus) for all terms [61]. The result is shown (orange) along with the Einstein model fit (black) in Fig. S7 [56]. As expected, the two models diverge at lower temperature. The strain $\Delta V/V$ (Fig. S8 [56]) is proportional to the squared magnetic moment, the order parameter, and reaches a value of 480×10^{-6} in the Einstein case and 320×10^{-6} in the Debye case, which are values commonly observed for similar magnetic moments [61].

E. Magnetic susceptibility

The discontinuity of the heat capacity at ≈ 75 K is in agreement with the AFM transition temperature of $75.5(8)$ K as obtained from the neutron-diffraction experiments. Also, the magnetic susceptibility measurement indicates AFM coupling below 75.4 K. A dominant AFM exchange interaction is evident from the magnetic susceptibility data. The broad maximum (disrupted below T_N) is characteristic for short-range AFM ordering in low-dimensional systems, i.e., an AFM coupled chain system. Above 200 K, the susceptibility can be modeled by a Curie-Weiss law with a Weiss constant of $\theta \approx 155(1)$ K (35 Oe) or $155.9(8)$ K (70 Oe) and a Curie constant of $C \approx 0.860(2)$, respectively $0.875(2)\text{ cm}^3\text{ K mol}^{-1}$, corresponding to an effective moment of $\mu_{\text{eff}} \approx 2.623(3)$, respectively $2.646(3)\mu_B$. The value of the Curie constant close to $1\text{ cm}^3\text{ K mol}^{-1}$ is g expected for a spin-only contribution from the d^2 ion Ru^{6+} with a Landé factor of $g \approx 1.855(2)$,

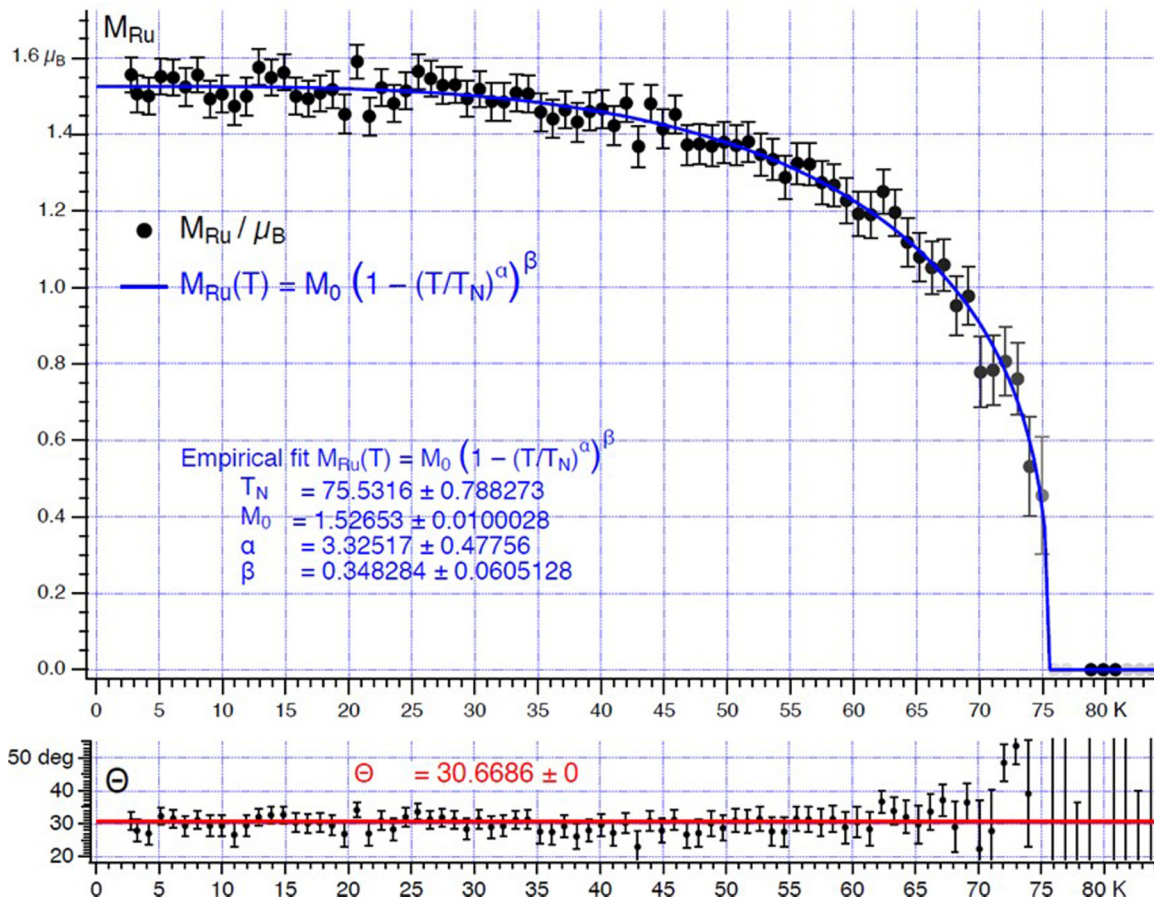


FIG. 8. Temperature dependence of the ordered Ru⁶⁺ magnetic moment magnitude in Ag₂RuO₄. Circles correspond to the results of the sequential refinement of a thermodiffraction. The solid blue line is a fit of the $M_{Ru}(T)$ data with Eq. (1) in the text. Below is shown the angle of the moment with respect to the c axis as a function of temperature.

respectively 1.871(2) and $S = 1$ [45]. From the Weiss temperature Θ one can deduce a model-free first estimate of the nearest exchange coupling through $-J_{\parallel} = 3k_B\Theta/[2zS(S+1)]$ with $z = 2$ nearest neighbors and spin $S = 1$. One obtains $J_{\parallel} = -58.0(3)$ K for 35 kOe, respectively $-58.5(3)$ K for 70 kOe. One notes that the Weiss constant is lower than the one found for Na₂RuO₄, indicating a weaker AFM exchange interaction. The obtained smaller value of g could be due to the effect of spin-orbit coupling and orbital contribution of the magnetic moment, as we discuss below.

Due to the considerable interchain interactions, resulting in long-range magnetic ordering, no attempt was made to fit an isolated Heisenberg chain model. In such a one, from $T(\chi_{\max}) \approx 76$ or 69 K (considering that, without long-range ordering, the maximum would lie at such a lower temperature) and $\chi_{\max} \approx 0.0033$ emu/mol, one would conclude, referring to Table 7.1 in Ref. [62], that $2J_{\parallel} \approx -56$ or -52 K and $g \approx 1.7$ or 1.6, respectively.

Below 200 K and above the Néel temperature of 76 K we attempted a fit of the susceptibility with a classical infinite chain model [63,64] in order to extract an estimate of the nearest-neighbor exchange parameter along the chains:

$$\chi = Ng^2\mu_B^2S(S+1)/3kT(1+u)/(1-u), \quad (3)$$

with $u = \coth[2J_{\parallel}S(S+1)/kT] - kT/[2J_{\parallel}S(S+1)]$.

The obtained exchange parameter of $2J_{\parallel} = -74(1)$ K (35 Oe), respectively $-73.81(8)$ K, and Landé factor $g = 1.7719(8)$, respectively 1.7854(6), are close to the values obtained for Na₂RuO₄ ($2J_{\parallel} = -86$ K) [45]. The deviation of g from 2 indicates presence of a low-level spin-orbit coupling but may as well be the result of the crude approximation of this $S = 1$ system by a classical spin-chain model. To obtain an estimate of the strength of the interchain coupling parameter $|2J_{\perp}|$ we use the following mean-field approximation [65]:

$$|2J_{\perp}| = T_N/\{1.28n[\ln(5.8|2J_{\parallel}|/T_N)]1/2\}. \quad (4)$$

With $n = 6$ neighboring chains, we obtain $|2J_{\perp}| \approx 7.5$ K. The sign of the interaction parameter cannot be evaluated, and as we deal with AFM and FM coupling between chains, as results from the neutron-diffraction study, we cannot elucidate it here. Also, we have to keep in mind that four neighboring chains are slightly closer (and couple mostly antiferromagnetically) and two are slightly further away (and couple exclusively ferromagnetically).

The ratio $2J_{\perp}/2J_{\parallel} \approx 10\%$ of inter- to intrachain exchange reflects the strong magnetic anisotropy in this material. The trigonal bipyramids coordinating ruthenium have a D_{3h} point symmetry and the axially elongated coordination results in singly occupied d_{yz} and d_{zx} orbitals (not degenerated due to the distortion of the trigonal bipyramids). The approximate 120° angle between the z axes of the orbital systems of two

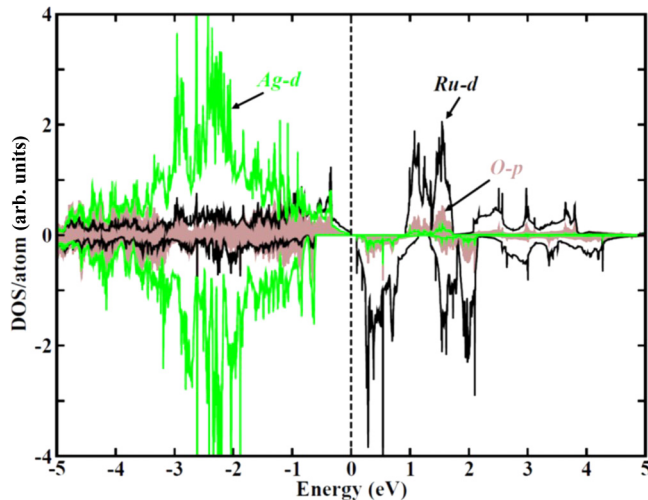


FIG. 9. GGA + U with $U_{\text{eff}} = 2$ eV spin-polarized density of states projected onto Ag-4d (light solid line), Ru-4d (dark line), and O-2p (filled) states. Two channels represent majority-spin (top) and minority-spin (bottom) channels. The Fermi level is marked at zero on the energy scale.

adjacent Ru^{6+} ions allows for sufficient overlap to produce an FM-AFM intrachain coupling by kinetic exchange.

F. Band structure and density of states

Figure 9 shows the electronic density of states (DOS) calculated within GGA + U ($U_{\text{eff}} = 2$ eV) for the FM state. The top and bottom panels show the majority- and minority-spin channels, respectively, while the Fermi energy is set at zero. Notably, even with inclusion of very small U at the Ru site the electronic structure shows an insulating solution with a very small gap of 0.1 eV. The Ag-4d states are completely filled in both spin channels, resulting in a nominal valance state of +1 for silver. The DOS shows that for Ru-4d states the majority-spin channel is partially filled and partially empty, whereas the minority-spin channel is completely empty. Due to the distorted nature of the trigonal bipyramidal [RuO_5] environment along with the tilting and rotation of the trigonal bipyramid along the apical direction, all d states are highly mixed up. Interestingly, there is substantial hybridization between O-2p states with Ru-4d states, as indicated by the overlap region in the DOS. The calculated magnetic moment at the Ru site is $1.17(1.33) \mu_B/\text{site}$ for $U_{\text{eff}} = 2(4)$ eV, while the total magnetic moment is $2 \mu_B/\text{f.u.}$

We crosschecked the band-structure calculations and the calculated exchange interactions for the range of U_{eff} from 1 to 4 eV. We found that for $U_{\text{eff}} = 1$ eV the electronic structure gives a metallic state, while for $U_{\text{eff}} > 1$ eV the band-structure calculation results in a gapped insulating state. We also found that for $U_{\text{eff}} = 2$ to 4 eV, apart from the increase in the magnetic moment at the Ru site and band gap, no major changes occurred in the electronic structure. Although the absolute value of the exchange interactions changes due to a change of U , the main trend remains unchanged. We also compared with the literature regarding the U value of the Ru, and we found that it is commonly assumed to lie between

2 and 3.5 eV [16,17,38,66–72]. The combination of DOS and calculated magnetic moment suggested that Ru in this material is in the +6 nominal valance state with $4d^2$ electronic configuration, with two states filled in the majority-spin channel and all remaining states in both spin channels being empty. Therefore, the underlying low-energy magnetic model of the present compound can be considered effectively as an $S = 1$ spin system. To understand the ground-state magnetic behavior of the said material better, we performed the total-energy investigation among different magnetic configurations of this effective $S = 1$ spin system. The effect of strong hybridization is also reflected by a substantially large induced magnetic moment at the oxygen sites of $0.14(0.1) \mu_B$ for $U_{\text{eff}} = 2(4)$ eV.

The experiments show clear indication of competition of both FM and AFM exchange interactions between different Ru sites. However, microscopically the individual nature of each different type of exchange interactions is not clear. Therefore, we calculated the magnetic exchange interactions between different Ru sites of the said material through a DFT based first-principles approach. Magnetic exchange interactions can be found using the extended Kugel-Khomskii model [73–75], following the knowledge of the orbital-dependent hopping interactions, on-site Hubbard U , and charge-transfer energies between different electronic states and orbitals. However, such an approach would require precise evaluation of the complicated hopping integral and charge-transfer energy among the different orbitals connected through complex superexchange pathways involving different types of atoms, which is hardly feasible for such an intricate material. Alternatively, one can calculate magnetic exchange interactions via the total-energy calculations and map the DFT total energies for different types of spin arrangements to the corresponding Ising-like model ($E^{\text{total}} = \sum_{ij} J_{ij} S_i^z S_j^z$) [75,76], where S_i^z 's are the effective spin value at the site i and j and J_{ij} is the exchange interaction between them. Although the total-energy calculation depends on the choice of Hubbard U , exchange correlation, etc., this method is able to provide the trends of exchange interactions reasonably well [75–79]. In the calculations, we consider the three most relevant isotropic exchange interaction (J 's) paths connecting different Ru sites. We considered intrachain superexchange interaction (J_1 ; $\angle \text{Ru-O-Ru} = 125.6^\circ$, Ru-Ru = 3.11 Å along the crystallographic a direction), interchain (J_2 ; Ru-Ru = 5.41 Å) in the crystallographic b - c plane, and interchain (J_3 ; Ru-Ru = 5.52 Å) along the crystallographic c direction, as illustrated in Fig. 10. The exchange interactions are calculated with $U_{\text{eff}} = 2$ eV. The total-energy calculations show the superexchange (Ru-O-Ru) intrachain (J_1) interaction is strongest (24.7 meV) and FM in nature, whereas the first neighbor interchain interaction (J_2) is AFM with a moderate strength of 18.1 meV. The next-neighboring interchain interaction (J_3) in the b - c plane is very weakly (1.6 meV) ferromagnetic, compared to J_1 and J_2 . Therefore, we can regard this compound to feature FM coupled chains running along the crystallographic a direction, which are coupled both antiferromagnetically (along the c direction) and ferromagnetically (in the diagonal bc plane). To understand the effect of Coulomb U on the calculated values of magnetic exchange interactions, we cross checked the J values for GGA + U_{eff} (=4 eV) and we found the trend to

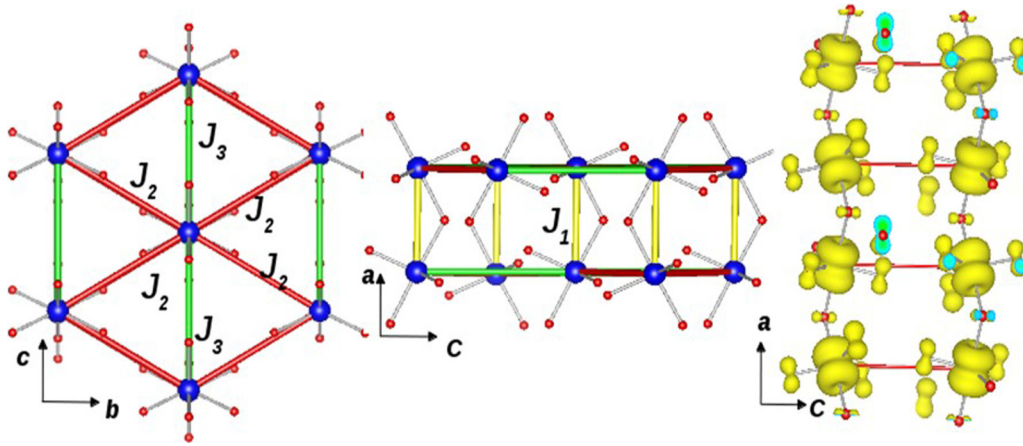


FIG. 10. The Ru only sublattice of Ag_2RuO_4 . Shown are the dominant exchange interactions paths J_1 (intrachain), J_2 , and J_3 (interchain) connecting between different Ru sites. The two figures on the left show two different view directions. Right panel: Three-dimensional magnetization density plot of Ag_2RuO_4 calculated through GGA + U . The isovalue was chosen to be $60 e^-/\text{\AA}^3$.

remain unaltered although the actual values of the exchange interactions [$J_1 = 20.4 \text{ meV}$ (FM), $J_2 = 11.1 \text{ meV}$ (AFM), $J_3 = 1.2 \text{ meV}$ (FM)] are changing.

The nature of the FM J_1 and AFM J_2 can be qualitatively understood from the Goodenough-Kanamori rules [80,81]. The superexchange angle connecting two Ru sites in the J_1 interaction path $\sphericalangle \text{Ru-O-Ru} = 125.64$ is far away from ideal 180° . Therefore, the FM component of the J_1 dominates over the AFM counterpart and finally stabilizes the ferromagnetic nature, whereas the in-plane canting of Ru spins induces the AFM nature for the J_2 interchain interaction.

To understand the orbital contribution to magnetic moment leading to a reduction of the g value, we calculated the electronic structure including spin-orbit coupling, i.e., GGA + U + SOC. We found a substantial orbital moment at the Ru site of around $0.033 \mu_B$ at $U_{\text{eff}} = 2 \text{ eV}$. We also calculated the magnetocrystalline anisotropy energy by aligning the spin quantization axis along [100], i.e., the chain direction and its perpendicular direction [001]. We found that this compound shows a strong easy axis [100] type of anisotropy (8.77 meV/f.u.). Thus, the small value of the obtained Landé g factor is due to the effect of a substantial orbital contribution toward the magnetic moment in addition to that of the spin part.

IV. DISCUSSION

Ag_2RuO_4 and Na_2RuO_4 feature astoundingly similar crystal structures. The primary building blocks are virtually identical, even quantitatively with respect to bond lengths and angles. Moreover, the secondary building units are virtually the same: $\text{RuO}_{3/1}\text{O}_{2/2}$ chains that are similarly oriented, packed, and corrugated. Finally, the tertiary structures are alike, where sodium and silver form approximate hexagonal tubes arranged like honeycombs, centered by the Ru/O chains. Even the local connectivity modes of chains provided by Ag and Na are similar. Noteworthy, Ag is not in its preferred linear coordination; instead it displays, like Na, a fivefold coordination.

The chains are arranged as pseudohexagonal rod packing in both structures, as shown in Figs. 4 and 5. Each chain, oriented in direction [100] for Ag_2RuO_4 , respectively [010] in Na_2RuO_4 [45], is surrounded by six neighbor chains while two of those show the same orientation, in direction [001] for Ag_2RuO_4 , respectively [101] for Na_2RuO_4 . Yet, there is a topological difference: While the chains in Ag_2RuO_4 are undulated in the same direction [001], i.e., the chains $[\text{Ru}-\text{O}_{\text{axial}}]_\infty$ lay in the plane formed by the chain direction [100] and [001], i.e., $(010)_{\text{ortho}}$, in Na_2RuO_4 the chains undulate in the plane $(100)_{\text{mono}}$, perpendicular rather than parallel to the direction in which chains look similar. Therefore, these “corrugation planes,” unite close chains with two (though the two farthest) of their six neighbor chains in Ag_2RuO_4 , whereas in Na_2RuO_4 they unite chains with two of the next-closest neighbors beyond the six closest ones (and, on top of that, with chains not containing the same symmetry-equivalent Ru ions). In both cases, the equatorial RuO_3 planes are perpendicular to that undulation (or corrugation) plane.

In terms of magnetic ordering, the two compounds differ even more significantly, see Fig. S6 and S9 [56]. In both cases the magnetic moment vectors lie in the equatorial RuO_3 planes. In Ag_2RuO_4 , in the corrugation plane $(010)_{\text{ortho}}$, while in Na_2RuO_4 they are perpendicular to the corresponding plane, $(100)_{\text{mono}}$. In Ag_2RuO_4 this corrugation plane is also the plane formed by equivalent next-neighbor chains. Chains inside these corrugation planes couple exclusively ferromagnetically.

Whereas in Na_2RuO_4 all magnetic moments are (nearly) parallel to each other, antiparallel between intrachain neighbors, and FM to next interchain neighbors, the magnetic moments in Ag_2RuO_4 are significantly inclined to each other, due to the topological difference of being parallel to the corrugation plane rather than perpendicular, while in both cases they are lying inside the equatorial RuO_3 planes.

Obviously, the subtle topological differences in the interchain arrangement could hold for explaining the rather different magnetic ordering schemes. However, as we expect the interchain interaction to be small, we shall have a close look at intrachain bond lengths and angles.

In Na_2RuO_4 we have Ru-Ru intrachain distances of 3.506 Å; distances to next-nearest neighbors are 5.315, 5.339, 5.418, and 5.464 Å plus twice 5.418 Å for Ru(1) and 5.506 Å for Ru(2). Equatorial Ru-O distances range from 1.753 to 1.782 Å; axial ones range from 1.974 to 2.000 Å. The O-Ru-O angle is 179.0° or 178.3°. The angle of the axis and the plane is 86.4° or 94.9°; the O-Ru-O angles in the plane range from 115.6° to 123.2°. The intrachain Ru-O-Ru angles are 124.1° or 122.7°. In Ag_2RuO_4 we find Ru-Ru intrachain distances of 3.543(2) Å; distances to next neighbors are twice 5.516(2) Å and four times 5.406(1) Å. Equatorial Ru-O distances are 1.767(3) Å and twice 1.776(2) Å; axial ones are 1.978(3) and 2.014(3) Å. The O-Ru-O angle is 179.9(2)°. The angle of the axis and the plane Ru-O bonds range from 85.8(2)° to 94.1(2)°; the O-Ru-O angles in the plane are twice 117.9(2)° to 124.2(2)°. The intrachain Ru-O-Ru angles are 125.1(1)°.

The bipyramids are equally distorted, the interchain distances are similar, and the intrachain corrugation angle Ru-O-Ru is larger by 0.8(8)%, respectively 2.0(8)%, but insignificantly. Only the Ru-Ru intrachain distance is significantly longer by 1.05(5)% in Ag_2RuO_4 .

This longer intrachain Ru-Ru distance despite similar bond distances and angles becomes obvious when regarding the connectivity between two coordination bipyramids in detail, as shown in Fig. S10 [56]. With the higher symmetry of Ag_2RuO_4 , together with the 3% larger unit-cell volume, apart from the “corrugation” angle Ru-O-Ru of 125°, the coordination bipyramids are perfectly “staggered,” i.e., an edge of one of the trigonal base planes (O3) is superposing a corner (O2) of a neighboring one. As a consequence, the oxygen positions forming this corner (O2) and this edge (O3) come with the corrugation angle so close on one side that they form a tetrahedron together with the oxygen position (O1) which links the two bipyramids. Due to the corrugation and the repulsion of the oxygen atoms forming the empty tetrahedron, the trigonal base plane of the stretched bipyramid is—in opposite direction to the magnetic moment, pointing out of a plane perpendicular to the axis by 2.3°—not exactly perpendicular to the bipyramid axis but inclined by 3.6° to a plane perpendicular to the axis. In total, the moment is inclined by 5.9° with respect to the plane spanned by O2 and O3. The O-O distances in the trigonal plane are $2 \times 3.064(2)$ Å for O2-O3 and 3.135(2) Å for O3-O3, the latter constituting the common edge with the empty tetrahedron. The O-O distances from the trigonal plane to the apical O1 position are 2.573(2) Å for O1-O2 and $2 \times 2.634(2)$ Å for O1-O3 not shared with the empty tetrahedron and 2.743(2) Å for O1-O2 and $2 \times 2.709(2)$ Å for O1-O3 shared with the tetrahedron, i.e., the longer bonds. The O-O distances in the empty tetrahedron are $2 \times 3.031(2)$ Å for O2-O3 (i.e., shorter than the O2-O3 distance of the bipyramid), in addition to the four distances evoked before, shared with the bipyramids. Shortest interchain O-O distances are 3.168(2) Å for O1-O2, $2 \times 3.125(1)$ Å for O2-O3, and 3.218(2) Å for O3-O3.

In Na_2RuO_4 the bipyramids are not staggered that “precisely” but “squeezed” into a less symmetric nearly staggered

conformation due to a lower unit-cell volume and incompressible Ru-O bond lengths. One may speculate here, whether the nuclear structure of Ag_2RuO_4 would transform to a similar lower symmetry when high pressure is applied, and with it the magnetic ordering.

It appears that the magnetic moment has two possible orientations, both roughly in the trigonal base plane: either pointing into the direction of the oxygen position forming the plane which is not part of the shared empty tetrahedron between bipyramids, as in the case of Ag_2RuO_4 , or roughly perpendicular to this, parallel to the edge of the trigonal plane shared with the empty tetrahedron, as in the case of Na_2RuO_4 . The latter results in a perfect AFM ordering scheme inside each chain, whereas the former leaves each chain with a consequence of the resulting magnetic moment to be compensated only by the perfect AFM arrangement of layers of FM ordered chains (Fig. S9 [56]).

V. CONCLUSIONS

Ag_2RuO_4 displays a trigonal bipyramidal coordination by oxygen for Ru^{6+} , which is rare in transition-metal oxide chemistry. These local building units are linked to form an effective infinite 1D quantum spin-chain system with $S = 1$. The oxoruthenate chains are arranged as an approximate hexagonal rod packing, significantly deviating from ideal trigonal symmetry, thus damping frustration effects commonly encountered with magnetic exchange on trigonal real space structures. As a consequence, this structural symmetry breaking results in a complex variety of electronic and magnetic interaction paths. While the intrachain coupling is clearly FM, the interchain couplings are either AFM or FM, sensitively depending on slight structural differences in mutual arrangements of and separations between the chains. However, the overall magnetic ordering is predominantly of AFM type. Although the title compound and sodium analog, Na_2RuO_4 , are very similar with respect to their crystal structure and valence electronic configuration, it comes as a surprise that the magnetic ordering schemes developed are substantially different, starting with the strongest intrachain coupling, which is AFM in Na_2RuO_4 , while all interchain exchange paths are FM in nature. Thus, the results obtained on the title compound, and direct comparison with very similar Na_2RuO_4 , are suited to demonstrate the effect on magnetic exchange couplings of only very gentle variations in the geometric detailing of the structures hosting interacting magnetic species.

ACKNOWLEDGMENTS

The authors acknowledge Dr. Walter Schnelle and Mr. Ralf Koban for magnetic, heat capacity, and resistivity measurements. S.K. thanks Department of Science & Technology, Government of India, for providing an INSPIRE faculty research grant (Grant No. DST/INSPIRE/04/2016/000431) and IUAC–New Delhi, India for providing computational facilities. S.S. thanks IIT Goa, Ministry of Human Resource Development, Government of India for providing a research fellowship.

- [1] A. Vasiliev, O. Volkova, E. Zvereva, and M. Markina, *npj Quantum Mater.* **3**, 18 (2018).
- [2] F. D. M. Haldane, *Phys. Rev. Lett.* **50**, 1153 (1983).
- [3] Z. Honda, H. Asakawa, and K. Katsumata, *Phys. Rev. Lett.* **81**, 2566 (1998).
- [4] D. C. Johnston, R. K. Kremer, M. Troyer, X. Wang, A. Klümper, S. L. Bud'ko, A. F. Panchula, and P. C. Canfield, *Phys. Rev. B* **61**, 9558 (2000).
- [5] S. Sachdev, *Quantum Phase Transitions* (Cambridge University, New York, 1999).
- [6] P. Lemmens, G. Güntherodt, and C. Gros, *Phys. Rep.* **375**, 1 (2003).
- [7] M. Hase, I. Terasaki, and K. Uchinokura, *Phys. Rev. Lett.* **70**, 3651 (1993).
- [8] S. Yamashita, Y. Nakazawa, M. Oguni, Y. Oshima, H. Nojiri, Y. Shimizu, K. Miyagawa, and K. Kanoda, *Nat. Phys.* **4**, 459 (2008).
- [9] M. Yamashita, N. Nakata, Y. Kasahara, T. Sasaki, N. Yoneyama, N. Kobayashi, S. Fujimoto, T. Shibauchi, and Y. Matsuda, *Nat. Phys.* **5**, 44 (2009).
- [10] C. Balz, B. Lake, J. Reuther, H. Luetkens, R. Schönemann, T. Herrmannsdörfer, Y. Singh, A. T. M. N Islam, E. M. Wheeler, A. Rodriguez-Rivera Jose, T. Guidi, G. Simeoni Giovanna, C. Baines, and H. Ryll, *Nat. Phys.* **12**, 942 (2016).
- [11] G. Jackeli and G. Khaliullin, *Phys. Rev. Lett.* **102**, 017205 (2009).
- [12] J. Chaloupka, G. Jackeli, and G. Khaliullin, *Phys. Rev. Lett.* **105**, 027204 (2010).
- [13] B. J. Kim, H. Ohsumi, T. Komesu, S. Sakai, T. Morita, H. Takagi, and T. Arima, *Science* **323**, 1329 (2009).
- [14] B. J. Kim, H. Jin, S. J. Moon, J. Y. Kim, B. G. Park, C. S. Leem, J. Yu, T. W. Noh, C. Kim, S. J. Oh, J. H. Park, V. Durairaj, G. Cao, and E. Rotenberg, *Phys. Rev. Lett.* **101**, 076402 (2008).
- [15] L. F. Mattheiss, *Phys. Rev. B* **13**, 2433 (1976).
- [16] S. Kanungo, R. Datta, and S. K. Panda, and T. Saha-Dasgupta, *J. Phys.: Condens. Matter* **25**, 505503 (2013).
- [17] E. Jakobi, S. Kanungo, S. Sarkar, S. Schmitt, and T. Saha-Dasgupta, *Phys. Rev. B* **83**, 041103(R) (2011).
- [18] G. Cao, S. McCall, M. Shepard, J. E. Crow, and R. P. Guertin, *Phys. Rev. B* **56**, 321 (1997).
- [19] J. J. Randall and R. Ward, *J. Am. Chem. Soc.* **81**, 2629 (1959).
- [20] L. Klein, J. S. Dodge, C. H. Ahn, J. W. Reiner, L. Mieville, T. H. Geballe, M. R. Beasley, and A. Kapitulnik, *J. Phys.: Condens. Matter* **8**, 10111 (1996).
- [21] J. M. Longo and P. M. Raccach, and J. B. Goodenough, *J. Appl. Phys.* **39**, 1327 (1968).
- [22] A. P. Mackenzie and Y. Maeno, *Rev. Mod. Phys.* **75**, 657 (2003).
- [23] K. W. Plumb, J. P. Clancy, L. J. Sandilands, V. V. Shankar, Y. F. Hu, K. S. Burch, H.-Y. Kee, and Y.-J. Kim, *Phys. Rev. B* **90**, 041112(R) (2014).
- [24] A. Banerjee, C. A. Bridges, J. Q. Yan, A. A. Aczel, L. Li, M. B. Stone, G. E. Granroth, M. D. Lumsden, Y. Yiu, J. Knolle, S. Bhattacharjee, D. L. Kovrizhin, R. Moessner, D. A. Tennant, D. G. Mandrus, and S. E. Nagler, *Nat. Mater.* **15**, 733 (2016).
- [25] A. Alexander, P. D. Battle, J. C. Burley, D. J. Gallon, C. P. Grey, and S. H. Kim, *J. Mater. Chem.* **13**, 2612 (2003).
- [26] W.-J. Son, P. Manuel, D. Adroja, and M.-H. Whangbo, *Inorg. Chem.* **50**, 9400 (2011).
- [27] M. D. Johannes, A. M. Stux, and K. E. Swider-Lyons, *Phys. Rev. B* **77**, 075124 (2008).
- [28] Y. Miura, Y. Yasui, M. Sato, N. Igawa, and K. Kakurai, *J. Phys. Soc. Jpn.* **76**, 033705 (2007).
- [29] K. Hoang, M. Oh, and Y. Choi, *ACS Appl. Electron. Mater.* **1**, 75 (2019).
- [30] H. Lux, *Z. Electrochem.* **45**, 303 (1939).
- [31] H. Flood and T. Forland, *Acta Chem. Scand.* **1**, 592 (1947).
- [32] C. Linke and M. Jansen, *Z. Anorg. Allg. Chem.* **623**, 1441 (1997).
- [33] M. Jansen, *J. Less Common Met.* **76**, 285 (1980).
- [34] M. Jansen, *Angew. Chem. Int. Ed.* **26**, 1098 (1987).
- [35] H. Schmidbaur and A. Schier, *Angew. Chem. Int. Ed.* **54**, 746 (2015).
- [36] B. U. Köhler, M. Jansen, and W. Weppner, *J. Solid State Chem.* **57**, 227 (1985).
- [37] C. Friebe and M. Jansen, *Z. Naturforsch. B* **39**, 739 (1984).
- [38] B. E. Prasad, S. Kanungo, M. Jansen, A. C. Komarek, B. Yan, P. Manuel, and C. Felser, *Chemistry—A European Journal* **23**, 4680 (2017).
- [39] W. Klein and M. Jansen, *Acta Crystallogr. C* **61**, i1 (2005).
- [40] B. E. Prasad, P. Kazin, A. C. Komarek, C. Felser, and M. Jansen, *Angew. Chem. Int. Ed.* **55**, 4467 (2016).
- [41] J. Darriet and J. Galy, *Bull. Soc. Fr. Mineral. Cristallogr.* **97**, 3 (1974).
- [42] M. Drillon, J. Darriet, and R. Georges, *J. Phys. Chem. Solids* **38**, 411 (1977).
- [43] J. T. Haraldsen, M. B. Stone, M. D. Lumsden, T. Barnes, R. Jin, J. W. Taylor, and F. Fernandez-Alonso, *J. Phys.: Condens. Matter* **21**, 506003 (2009).
- [44] K. M. Mogare, K. Friese, W. Klein, and M. Jansen, *Z. Anorg. Allg. Chem.* **630**, 547 (2004).
- [45] K. M. Mogare, D. V. Sheptyakov, R. Bircher, H.-U. Güdel, and M. Jansen, *Eur. Phys. J. B* **52**, 371 (2006).
- [46] M. Shikano, R. K. Kremer, M. Ahrens, H. J. Koo, M. H. Whangbo, and J. Darriet, *Inorg. Chem.* **43**, 5 (2004).
- [47] A. Balodhi and Y. Singh, *Phys. Rev. Mater.* **2**, 024403 (2018).
- [48] G. Nowogrocki, Sur le comportement en solution aqueuse des valences supérieures du ruthénium, Thèse Docteur ès Sciences, Université Lille1 (1967).
- [49] Bruker AXS, TOPAS, Version 4.2 (Bruker AXS Inc., Madison, WI, 2009).
- [50] T. C. Hansen, P. F. Henry, H. E. Fischer, J. Torregrossa, and P. Convert, *Meas. Sci. Technol.* **19**, 034001 (2008).
- [51] G. Kresse and J. Hafner, *Phys. Rev. B* **47**, 558 (1993).
- [52] G. Kresse and J. Furthmüller, *Phys. Rev. B* **54**, 11169 (1996).
- [53] J. P. Perdew, K. Burke, and M. Ernzerhof, *Phys. Rev. Lett.* **77**, 3865 (1996).
- [54] V. I. Anisimov, I. V. Solovyev, M. A. Korotin, M. T. Czyżyk, and G. A. Sawatzky, *Phys. Rev. B* **48**, 16929 (1993).
- [55] S. L. Dudarev, G. A. Botton, S. Y. Savrasov, C. J. Humphreys, and A. P. Sutton, *Phys. Rev. B* **57**, 1505 (1998).
- [56] See Supplemental Material at <http://link.aps.org/supplemental/10.1103/PhysRevMaterials.4.024418> for TGA/DTA data, susceptibility data, electrical resistivity data, structure plots, neutron-diffraction patterns taken at a wavelength of 2.41 Å at 1.8 and 76 K, projection of the magnetic structure of Na₂RuO₄, lattice constants and unit-cell volume as a function of temperature with Einstein model fit above T_N, plot of the volume strain as a function of the squared magnetic moment, and table of atomic parameters.
- [57] M. Hillert and M. Jarl, *Calphad* **2**, 227 (1978).

- [58] T. Roisnel and J. Rodríguez-Carvajal, *Mater. Sci. Forum* **378–381**, 118 (2001).
- [59] J. Rodríguez-Carvajal, *IUCR-CPD Newsl.* **26**, 12 (2001).
- [60] I. S. Anderson, P. J. Brown, J. M. Carpenter, G. Lander, R. Pynn, J. M. Rowe, O. Schärpf, V. F. Sears, and B. T. M. Willis, *Neutron Techniques International Tables for Crystallography Mathematical, Physical and Chemical Tables Vol. C* (International Union of Crystallography, Chester, England, 2006), pp. 430–87.
- [61] T. Chatterji and T. C. Hansen, *J. Phys.: Condens. Matter* **23**, 276007 (2011).
- [62] R. L. Carlin, *Magnetochemistry* (Springer-Verlag, Berlin, 1986).
- [63] M. E. Fisher, *Am. J. Phys.* **32**, 343 (1964).
- [64] O. Kahn, *Molecular Magnetism* (VCH, New York, 1993).
- [65] A. N. Vasiliev, O. L. Ignatchik, M. Isobe, and Y. Ueda, *Phys. Rev. B* **70**, 132415 (2004).
- [66] H. T. Dang, J. Mravlje, A. Georges, and A. J. Millis, *Phys. Rev. B* **91**, 195149 (2015).
- [67] J. Mravlje, M. Aichhorn, T. Miyake, K. Haule, G. Kotliar, and A. Georges, *Phys. Rev. Lett.* **106**, 096401 (2011).
- [68] Z. V. Pchelkina, I. A. Nekrasov, Th. Pruschke, A. Sekiyama, S. Suga, V. I. Anisimov, and D. Vollhardt, *Phys. Rev. B* **75**, 035122 (2007).
- [69] S. Ryee and M. J. Han, *Sci. Rep.* **8**, 9559 (2018).
- [70] M. H.-E. Musa Saad, *Mater. Chem. Phys.* **204**, 350 (2018).
- [71] R. Bentata, S. Bentata, B. Bouadjemi, T. Lantri, and D. Chenine, *Chin. J. Phys.* **59**, 28 (2019).
- [72] C. Gauvin-Ndiaye, A.-M. S. Tremblay, and R. Nourafkan, *Phys. Rev. B* **99**, 125110 (2019).
- [73] K. I. Kugel and D. I. Khomskii, *Zh. Eksp. Teor. Fiz.* **64**, 1429 (1973) [*Sov. Phys. JETP* **37**, 725 (1973)].
- [74] K. I. Kugel and D. I. Khomskii, *Sov. Phys. Usp.* **25**, 231 (1982).
- [75] V. V. Mazurenko, F. Mila, and V. I. Anisimov, *Phys. Rev. B* **73**, 014418 (2006).
- [76] C. S. Hellberg, W. E. Pickett, L. L. Boyer, H. T. Stokes, and M. J. Mehl, *J. Phys. Soc. Jpn.* **68**, 3489 (1999).
- [77] S. Kanungo, B. Yan, M. Jansen, and C. Felser, *Phys. Rev. B* **89**, 214414 (2014).
- [78] S. Kanungo, B. Yan, C. Felser, and M. Jansen, *Phys. Rev. B* **93**, 161116(R) (2016).
- [79] J. Sannigrahi, J. Sichelschmidt, B. Koo, A. Banerjee, S. Majumdar, and S. Kanungo, *J. Phys.: Condens. Matter* **31**, 245802 (2019).
- [80] J. B. Goodenough, *Phys. Rev.* **100**, 564 (1955).
- [81] J. B. Goodenough, *Magnetism and the Chemical Bond* (Interscience, New York, 1963).